Banner appropriate to article type will appear here in typeset article

Collapse of statistical equilibrium in large-scale hydroelastic turbulent waves

Marlone Vernet and Eric Falcon†

Université Paris Cité, CNRS, MSC, UMR 7057, F-75 013 Paris, France

At scales larger than the forcing scale, some out-of-equilibrium turbulent systems (such as hydrodynamic turbulence, wave turbulence, and nonlinear optics) exhibit a state of statistical equilibrium where energy is equipartitioned among large-scale modes, in line with the Rayleigh-Jeans spectrum. Key open questions now pertain to either the emergence, decay, collapse, or other nonstationary evolutions from this state. Here, we experimentally investigate the free decay of large-scale hydroelastic turbulent waves, initially in a regime of statistical equilibrium. Using space- and time-resolved measurements, we show that the total energy of these large-scale tensional waves decays as a power law in time. We derive an energy decay law from the theoretical initial equilibrium spectrum and the linear viscous damping, as no net energy flux is carried. Our prediction then shows a good agreement with experimental data over nearly two decades in time, for various initial effective temperatures of the statistical equilibrium state. We further identify the dissipation mechanism and confirm it experimentally. Our approach could be applied to other decaying turbulence systems, with the large scales initially in statistical equilibrium.

Key words: Hydroelastic waves, Statistical Equilibrium, Decaying turbulence, Experiments

1. Introduction

The possible coexistence of two distinct regimes in out-of-equilibrium (forced and dissipated) turbulent systems, namely, a turbulent cascade at small scales and statistical equilibrium (SE) at large scales, is particularly interesting. It suggests that classical tools from statistical mechanics may be applicable for describing the large-scale behavior of turbulent systems. In this context, "large scales" refer to scales larger than the forcing scale, and SE is characterized by energy equipartition among degrees of freedom due to the absence of flux across large scales. Evidence of SE at large scales has been reported in different systems, including three-dimensional (3D) hydrodynamic turbulence (Gorce & Falcon 2022), capillary wave turbulence (Michel et al. 2017), flexural wave turbulence (Miquel et al. 2021), and hydroelastic wave turbulence (Vernet & Falcon 2025). Classical condensation toward SE has also been reported in optics (Sun et al. 2012; Baudin et al. 2020).

While the existence of SE within out-of-equilibrium systems is appealing, many questions

Abstract must not spill onto p.2

remain. In particular, what is the mechanism to reach the SE regime, and how does it grow or decay upon the starting or stopping of external forcing? How do the regimes of statistical equilibrium (at large scales) and out-of-equilibrium (at small scales) interact, since they are not isolated from each other? These questions, in this context, involve nonstationary processes that are central to understanding how stationary regimes in physics arise and collapse.

Numerous studies have focused on the decay processes in nonlinear out-of-equilibrium systems, including 3D hydrodynamic turbulence in wind tunnels (Comte-Bellot & Corrsin 1966) and rotating turbulence (Morize & Moisy 2006), initially forced at a large scale. Free decay has also been investigated in two-dimensional (2D) turbulence, in a soap film (Martin et al. 1998; Cieślik et al. 2009), in fluid layers (Shats et al. 2010), in electron plasma (Bettega & Roman 2009), in 3D magnetohydrodynamics turbulence (Bigot et al. 2008; Beresnyak & Lazarian 2008), and quantum turbulence (Skrbek & Sreenivasan 2012). In the context of wave turbulence, decay dynamics have been explored numerically for surface gravity waves (Onorato et al. 2002; Yokoyama 2004; Zhang & Pan 2022) and capillary waves (Falkovich et al. 1995; Pan & Yue 2015) and experimentally for elastic waves in a thin plate (Miquel & Mordant 2011), hydroelastic waves (Deike et al. 2013), surface gravity (Bedard et al. 2013; Deike et al. 2015), gravity-capillary (Cazaubiel et al. 2019) and capillary (Kolmakov et al. 2004; Deike et al. 2012) waves.

While all these nonstationary studies focused on the free decay of small-scale turbulent cascade (primarily investigating whether the constant energy-flux phenomenology persists), only a few have examined the decay behavior of large scales that initially exhibit a SE regime. In particular, a recent experiment on 3D turbulence, initially forced at a small scale, was able to distinguish between Saffman's and Batchelor's models of freely decaying turbulence, in the early stage and final decay regimes (Gorce & Falcon 2024).

Hydroleastic waves are of particular interest, as they are deformation modes of an elastic plate in contact with a fluid. These waves have direct applications in oceanography, notably in modeling wave propagation over ice-covered ocean surfaces (Davys et al. 1985; Sutherland et al. 2016; Das et al. 2018; Pǎrǎu et al. 2024). The need for a better understanding of hydroelastic wave dynamics has grown in recent years with the emergence of very large floating structures, such as mobile offshore bases and expansive floating solar farms (Wang et al. 2008; Yang & Huang 2024).

Here, we experimentally investigate how large-scale hydroelastic turbulent waves, initially in SE, freely decay when external small-scale forcing is stopped. This decay is then understood using a simple model based on the energy budget in Fourier space and on the dissipation mechanism at play.

2. Experimental setup

The experimental setup follows that of Vernet & Falcon (2025) and is shown in figure 1. It consists of a square tank of dimensions $L \times L \times h$ with $L = 600$ mm and $h = 100$ mm. The tank is fully filled with water (density $\rho = 10^3$ kg m^{-3}) and covered by a white elastic sheet made of silicone rubber (Ecoflex 00-30 soft elastomer) of thickness $e = 0.5$ mm, density $\rho_s \simeq 10^3$ kg m^{-3}, Young's modulus $E_Y = 7 \times 10^4$ Pa and Poisson's coefficient $\tilde{\nu} \approx 0.5$ (Delory et al. 2024). A solid ring is placed on the top of the sheet to apply circular boundary conditions and to enhance multidirectional wave reflections. The tank is connected to a column filled with water to control the imposed hydrostatic pressure in the liquid and the sheet stretching, and thus the applied tension $T \in [3, 7]$ N m^{-1} to the sheet. Hydroelastic waves are produced by the vertical motion of a disk-shaped wavemaker (50 mm in diameter) driven by an electromagnetic shaker (LDS V406) fed with a bandpass-filtered Gaussian random noise signal in the range $f_p \in [50, 100]$ Hz. The vertical deformations of the sheet
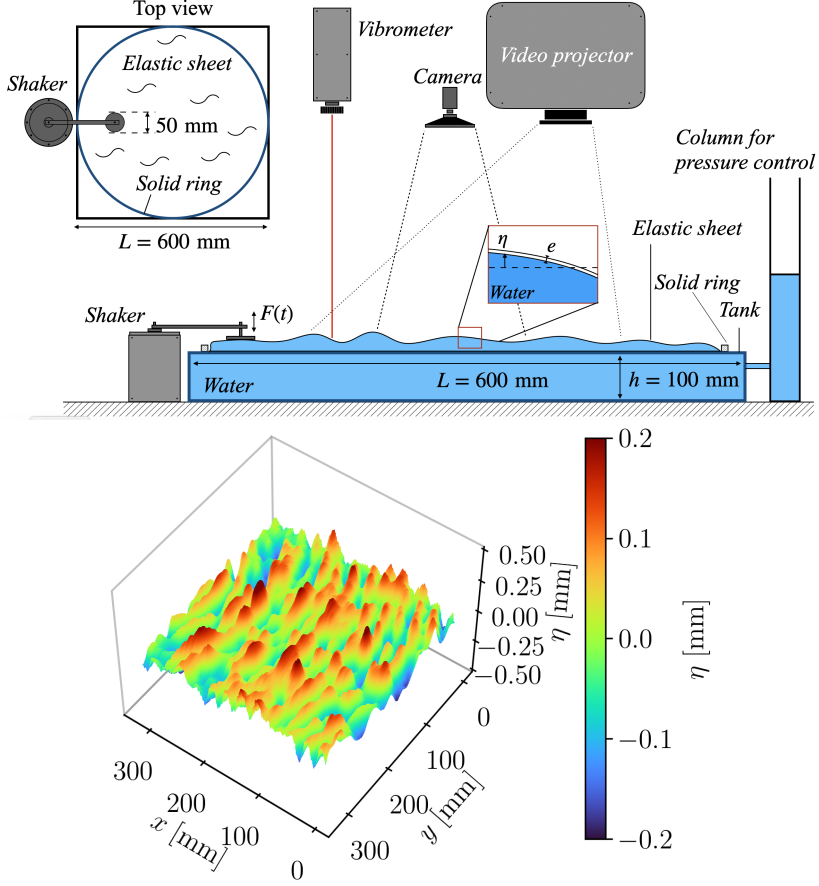
Figure 1: Top: Scheme of the experimental setup to study hydroelastic waves (lateral view). Left: top view. Bottom: Typical hydroelastic wave field, $\eta(x, y)$, obtained from Fourier transform profilometry.

are either measured at a given position, $\xi(t)$, with a laser Doppler vibrometer (Polytech OFV5000-505) or are fully resolved in space and time, $\eta(x, y, t)$, using the Fourier transform profilometry (FTP) method (Cobelli et al. 2009) using a camera (Basler acA2040) recording at 120 fps the deformations of a fringe pattern projected over the sheet by a full-HD video projector (Epson EH-TW9400). The size of the recorded images, centered in the middle of the sheet, is $\mathcal{L}^2 = 300 \times 300$ mm^2. The sampling frequency of the vibrometer is 2 kHz. The two notations ξ and η thus refer to the two experimental methods that yield the sheet vertical deformations.

The two measurements are not performed simultaneously due to technical reasons. In both cases, measurements are started at $t = 0$ when the wave maker is turned on to capture the statistical equilibrium regime of the large scales (reached in about 1 s). At t_0, it is switched off to record the free decay. The same experiment is repeated 60 times, in the vibrometer case, to obtain an ensemble average, thereby increasing statistics, reducing the signal-to-noise ratio, and improving the time-frequency analysis. This one-point measurement is used to perform a time-frequency analysis of the decay lasting ~ 20 s. The spatiotemporal measurement gives access to the spatial decay of the Fourier modes for $t \geqslant t_0$ and the dispersion relation for $t < t_0$. Typical wave amplitude is [0.1, 1] mm in the SE regime.
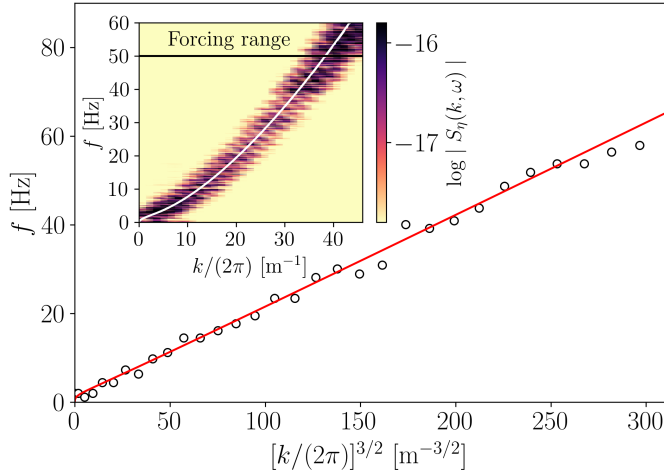
Figure 2: Experimental dispersion relation f versus $[k/(2\pi)]^{3/2}$ (black circle). Small-scale random forcing $f_p \in [50, 100]$ Hz. Red line: polynomial fit of Eq. (3.1) with only one fitting parameter, the tension T, which yields $T = 6.8$ N m^{-1}. Inset: Spatiotemporal spectrum of the wave height, $S_\eta(k, \omega)$, versus $f \equiv \omega/(2\pi)$ and $k/(2\pi)$. Solid white line: linear dispersion relation of Eq. (3.1). Black line: lower bound [min(f_p)] of the random forcing range.

3. Results

3.1. Hydroelastic waves

Hydroelastic waves are deformations of an elastic sheet covering a fluid. They are described by combining two equations, coupling elasticity and hydrodynamics. The Föppl-von Kármán equation expresses the dynamics of the vertical deformation $\eta(x, y, t)$ of a thin elastic sheet while Bernoulli's theorem yields the pressure field exerted by a perfect fluid on the sheet (Landau & Lifshitz 1970). Neglecting sheet inertia ($ke \ll \rho/\rho_s$ with ρ the fluid density), the dispersion relation of hydroelastic waves, in a deep water regime ($kh \gg 1$ with fluid depth h), reads (Davys et al. 1985; Schulkes et al. 1987; Deike et al. 2013)

$$\omega^2 = gk + \frac{T}{\rho}k^3 + \frac{B}{\rho}k^5, \tag{3.1}$$

where ω is the wave angular frequency, k is the wave number modulus, g is the gravity acceleration, T is the externally applied tension, and $B = E_Y e^3/[12(1 - \tilde{\nu}^2)] \simeq 9.7 \; 10^{-7}$ N m is the bending modulus. The three terms of the right-hand side of Eq. (3.1) correspond to gravity waves, tensional waves, and flexural waves, respectively.

The dispersion relation is reached experimentally from the wave field, $\eta(x, y, t)$, given by the FTP method. We compute the Fourier transform in space $\check{\eta}(k_x, k_y, t)$ which leads in polar coordinates to $\check{\eta}(k, \varphi, t)$ with $k = (k_x^2 + k_y^2)^{1/2}$ and $\varphi \in [0, 2\pi[$. The Fourier transform in time of this field gives $\hat{\eta}(k, \varphi, \omega)$ which is used to compute the spatiotemporal spectrum $S_\eta(k, \omega) = \langle |\hat{\eta}(k, \varphi, \omega)|^2 \rangle_\varphi / (\mathcal{L}^2 \mathcal{T})$, with $\mathcal{L}$ the window length and $\mathcal{T} = 30$ s the acquisition time. The spatiotemporal spectrum, $S_\eta(k, \omega)$, of the wave field, $\eta(x, y, t)$, is shown in the inset of figure 2. A small-scale random forcing is applied in the range $f_p \in [50, 100]$ Hz. We observe that wave energy is spread over all scales larger than the forcing scales (i.e., $f < f_p$), around the theoretical dispersion relation of Eq. (3.1) (white line). The experimental dispersion relation is then inferred from the $S_\eta(k, \omega)$ maximum value for each k as shown in the main figure 2 (black circle). Experimental data exhibit a clear $k^{3/2}$ power law, highlighting the tensional nature of the waves over the f and k available ranges. Experimental data are then

fitted by a polynomial fit of Eq. (3.1) to infer the sheet tension T. Note that from Eq. (3.1), the crossover between gravity and tension waves is $k_{gt} = \sqrt{\rho g/T}$, and between bending and tension waves, $k_{bt} = \sqrt{T/B}$, which give $k_{gt}/(2\pi) \simeq 6$ m^{-1} and $k_{bt}/(2\pi) \simeq 421$ m^{-1}, respectively. Gravity is thus relevant for wavelengths longer than ~ 16 cm, whereas bending effects occur at scales much smaller than the forcing scale, thus confirming the tensional nature of the waves in the window of interest.

3.2. *Statistical equilibrium (Rayleigh-Jean spectrum)*

Statistical equilibrium corresponds to a stationary state where energy is equally shared among different modes of a system. For 2D isotropic systems, such equipartition of kinetic energy among Fourier modes $\mathbf{k}$ leads to the theoretical energy spectrum (Zakharov et al. 2025)

$$E^{\mathrm{Eq}}(k) = \frac{k_B \theta}{2\pi \rho} k, \qquad (3.2)$$

where $k \equiv ||\mathbf{k}||$, k_B is the Boltzmann constant and θ is an effective temperature. Using $E^{\mathrm{Eq}}(k)dk = E^{\mathrm{Eq}}(\omega)d\omega$, and Eq. (3.1) considering only tensional waves, the energy spectrum of statistical equilibrium of large-scale hydroelastic tensional waves reads

$$E^{\mathrm{Eq}}(\omega) = \frac{k_B \theta}{3\pi \rho^{1/3} T^{2/3}} \omega^{1/3}. \qquad (3.3)$$

Note that the energy spectrum is related to the wave amplitude power spectrum, $S(k)$, by $E(k) = (T/\rho)k^2 S(k)$ and $E(\omega) = (T/\rho)^{1/3}\omega^{4/3}S(\omega)$ for pure tensional waves. Such a statistical equilibrium regime of large-scale hydroelastic tensional waves has been experimentally evidenced by Vernet & Falcon (2025) (see also Sect. 3.5). Hereafter, as θ is no longer discussed, we will use $E_0 \equiv k_B\theta$ as the SE energy reference.

3.3. *Free decay from a statistical equilibrium regime*

We now focus on the free decay of a system initially in a statistical equilibrium regime, once the forcing is stopped, to understand how the energy stored in large scales is damped. To do so, we adapt to our case the model of decay of 3D hydrodynamics turbulence Batchelor (1953); Saffman (1967); Gorce & Falcon (2024).

The energy budget in ω-Fourier space reads

$$\frac{\partial E(\omega, t)}{\partial t} = T(\omega, t) + I(\omega, t) - D(\omega, t), \qquad (3.4)$$

where $E(\omega, t)$ is the energy spectral density, $T(\omega, t)$ is the energy transfer between waves (nonlinear term), $I(\omega, t)$ denotes the injected power, and $D(\omega, t)$ the spectral dissipation (linear term). In the stationary state, dissipation is negligible compared to nonlinearities within the large scales. As soon as the Rayleigh-Jean spectrum is established, the mean energy flux vanishes at large scales. This does not exclude positive or negative fluctuations of the energy flux, which are the counterpart of the fluctuations of the injected power, as observed for the large scales in SE in hydrodynamic turbulence (Gorce & Falcon 2022). Once the external forcing is turned off at $t = t_0$, one has $I = 0$ and the wave field then freely decays over time, in two stages.

(i) First, an initial decay dominated by reminiscent nonlinear processes, which lasts as long as the energy transfer towards small scales occurs in the inertial range (Batchelor 1953; Comte-Bellot & Corrsin 1966; Gorce & Falcon 2024). During this initial decay, energy exchange between small scales and large scales still occurs through nonlinear transfer, thus maintaining the SE regime during that period.

(ii) Then, the final decay starts when nonlinearities become negligible, such that the viscous dissipation dominates the decay dynamics at all scales.

Due to the time resolution limitation of the time-frequency analysis in Sect 3.4, we can not accurately characterize the initial decay. Thus, hereafter, we focus only on the final decay which starts at time t_ν, larger than t_0. Experimentally, t_ν is the time at which the spectrum departs from the SE prediction of Eq. (3.3).

In the final decay, Eq. (3.4) then reads

$$\frac{\partial E(\omega,t)}{\partial t} = -D(\omega,t) \equiv -\frac{2}{\tau(\omega)}E(\omega,t), \tag{3.5}$$

where $\tau(\omega)$ is the typical linear dissipation time scale. The term on the right-hand side thus corresponds to energy dissipation induced by a linear mechanism. The factor 2 comes from the definition of τ from the exponential decay $\xi(t) \equiv \xi_\nu e^{-(t-t_\nu)/\tau}$ with $\xi_\nu \equiv \xi(t = t_\nu)$ as t_ν is the final decay starting time. By integrating Eq. (3.5) between t_ν and t, the energy decays exponentially as

$$E(\omega,t) = E(\omega,t_\nu)e^{-\frac{2}{\tau(\omega)}(t-t_\nu)}. \tag{3.6}$$

As long as the final decay is not reached ($t \leqslant t_\nu$), we assume that the energy spectrum of the large scales follows a frequency power law. Thus, at time $t = t_\nu$, one assumes $E(\omega,t_\nu) = A\omega^\alpha$ with A a constant. The exponent α is kept for the sake of generality, but one can bear in mind that, from Eq. (3.3), $\alpha = 1/3$ and $A \equiv E_0/[3\pi(\rho T^2)^{1/3}]$ in our case. Inserting $E(\omega,t_\nu)$ into Eq. (3.6), and the result into the total energy at time t, $\mathcal{E}_{th}^\omega(t) \equiv \int_0^{\omega_c} E(\omega,t)d\omega$, yields

$$\mathcal{E}_{th}^\omega(t) = \int_0^{\omega_c} A\omega^\alpha e^{-\frac{2}{\tau(\omega)}(t-t_\nu)}d\omega \ \text{ for } t \geqslant t_\nu. \tag{3.7}$$

The superscript indicates whether total energy is computed from the frequency spectrum ($\mathcal{E}^\omega$) or the spatial spectrum ($\mathcal{E}^k$) afterwards, while the index "th" indicates a theoretical expression. ω_c is a high-frequency cutoff that prevents the divergence of the integral at $t = t_\nu$ and which appears naturally since SE is observed for frequencies smaller than forcing frequencies f_p.

Let us assume that $\tau(\omega)$ is a power-law function of ω (as justified afterwards) as $\tau(\omega) = 2/(C\omega^\beta)$ where the exponent β and the positive constant C depend on the dissipation mechanism (see Sect. 3.4). The integral of Eq. (3.7) is convergent if $\alpha > -1$ to ensure the convergence when ω tends to zero. Using the change of variable ω by $C(t-t_\nu)\omega^\beta$ in Eq. (3.7), we obtain a prediction for the decay of the total energy as

$$\mathcal{E}_{th}^\omega(t) = \tilde{A}(t - t_\nu)^{-\delta}\gamma[\delta,(t - t_\nu)/\tau_c], \tag{3.8}$$

where $\delta = (\alpha+1)/\beta$ is the time power-law exponent, $\tilde{A} = AC^{-\delta}/\beta$ is a constant, $\tau_c = \tau(\omega_c)/2$, and γ is the lower incomplete Gamma function, $\gamma[s,x] \equiv \int_0^x u^{s-1}e^{-u}du$. When $t \to t_\nu$, Taylor's expansion of γ scales as $\gamma[\delta,(t-t_\nu)/\tau_c] \propto (t-t_\nu)^\delta$ and thus regularizes Eq. (3.8), i.e., prevents the divergence of $\mathcal{E}_{th}^\omega(t)$. When $x \to +\infty$, $\gamma[s,x]$ tends to $\Gamma(s)$, the usual Euler's Gamma function. The error between the two functions, $\gamma[s,x]$ and $\Gamma(s)$, is of the order $O(x^{s-1}e^{-x})$. Thus, $\mathcal{E}_{th}^\omega(t)$ is predicted to follow a time power law for $(t - t_\nu) > \tau_c$, as

$$\mathcal{E}_{th}^\omega(t) \simeq \tilde{A}(t - t_\nu)^{-\delta}\Gamma(\delta). \tag{3.9}$$

This approximation will be discussed later in the light of the experimental values of τ_c.

Thus, although all energy modes $E(\omega,t)$ follow exponential decays of Eq. (3.6), the total energy $\mathcal{E}_{th}^\omega(t)$ decreases accordingly to a time power-law of Eq. (3.9).

This result appears to be quite general and extends beyond the scope of hydrodynamic

turbulence and wave turbulence. Indeed, if the energy spectrum of a system, initially follows a frequency power-law, and decays over time accordingly to a relation analog to Eq. (3.5), then the total energy will decay as a time power-law as Eq. (3.9) whose the exponent δ can be predicted as long as the linear time scale $\tau(\omega)$ is a frequency power-law function.

In our specific case of hydroelastic tensional waves where large scales are initially in a statistical equilibrium regime, with a spectrum as in Eq. (3.3), one has $\alpha = 1/3$ and $A \equiv E_0/[3\pi(\rho T^2)^{1/3}]$. Moreover, the linear dissipation time $\tau(\omega)$ is predicted to scale as $\tau(\omega) = 2/(C\omega^\beta)$ with $\beta = 7/6$ and $C \equiv \sqrt{\nu/2}(\rho/T)^{1/3}$ [see Sect. 3.4 and Eq. (3.11)]. Therefore, the prediction for the total energy decay reads, from Eq. (3.9),

$$\mathcal{E}_{\text{th}}^\omega(t) \simeq \frac{2^{11/7}\Gamma(8/7)\,E_0}{7\pi(\nu^4\rho^5 T^2)^{1/7}}(t - t_\nu)^{-8/7}, \tag{3.10}$$

that is $\delta = (\alpha + 1)/\beta = 8/7$ and $\tilde{A} = AC^{-\delta}/\beta = 2^{11/7}E_0/[7\pi\rho^{5/7}T^{2/7}\nu^{4/7}]$ using previous notations.

Before testing experimentally in Sect. 3.5 the large-scale energy decay prediction of Eq. (3.10), the viscous dissipation nature of hydroelastic tensional waves is first investigated below (Sect. 3.4), as it prescribes the β exponent value.

3.4. *Viscous dissipation time scale*

To obtain the exponent β, one must explore the dissipation mechanism in the system. For a plate in contact with a liquid, the boundary condition of zero tangential displacement can be obtained in two limits. In the small wave-amplitude limit, the sheet thickness is greater than the displacements of points in the sheet, which guarantees the existence of a neutral surface. On that surface, there is no compression or extension, and the horizontal displacements vanish at first order (§11 of Landau & Lifshitz (1970)). This condition generally holds for an ice layer covering the ocean (Squire 2009). Here, the wave amplitude is of the order of the typical sheet thickness $e = 0.5$ mm (see bottom of figure 1). However, applying an external pressure is crucial as the stress tensor is dominated by the constant external stretching forces (§14 of Landau & Lifshitz (1970)). In consequence, also dynamical horizontal displacement of the sheet is also expected here, and we thus assume a zero tangential velocity boundary condition at the sheet/liquid interface. The derivation of the dissipation time scale is then fully analogous to the deep-water surface wave case. In that case, the air/liquid surface boundary layer is due to an inextensible film (Lamb 1932; Miles 1967), with $\tau^{-1}(\omega) = k\sqrt{\omega\nu}/(2\sqrt{2})$, and $\omega(k)$ given by the gravity-capillary wave dispersion relation. For hydroelastic tensional waves, $\omega(k)$ is given by the second term of the right-hand side of Eq. (3.1), and the same procedure yields a similar expression for $\tau(\omega)$ as

$$\tau^{-1}(\omega) = \frac{\nu^{1/2}}{2\sqrt{2}}\left(\frac{\rho}{T}\right)^{1/3}\omega^{7/6}. \tag{3.11}$$

and thus to the exponent $\beta = 7/6$.

Let us experimentally check the prediction of Eq. (3.11) for the frequency-power law of the dissipation time scale, $\tau(\omega)$, and the corresponding exponential decay of the energy spectral density $E_\xi(\omega, t)$ of Eq. (3.6). $E_\xi(\omega, t)$ is obtained by performing a time-frequency analysis, i.e., a spectrogram of the temporal signal of the pointwise vertical position $\xi(t)$ (see inset of figure 3a) measured by the vibrometer. The spectrogram is computed as the power-spectral density at each time t^*

$$S_\xi(\omega, t^*) \equiv \int_{t^*}^{t^*+\delta t} \langle\xi(t)\xi(t + s)\rangle_t e^{-i\omega s}\,ds \tag{3.12}$$
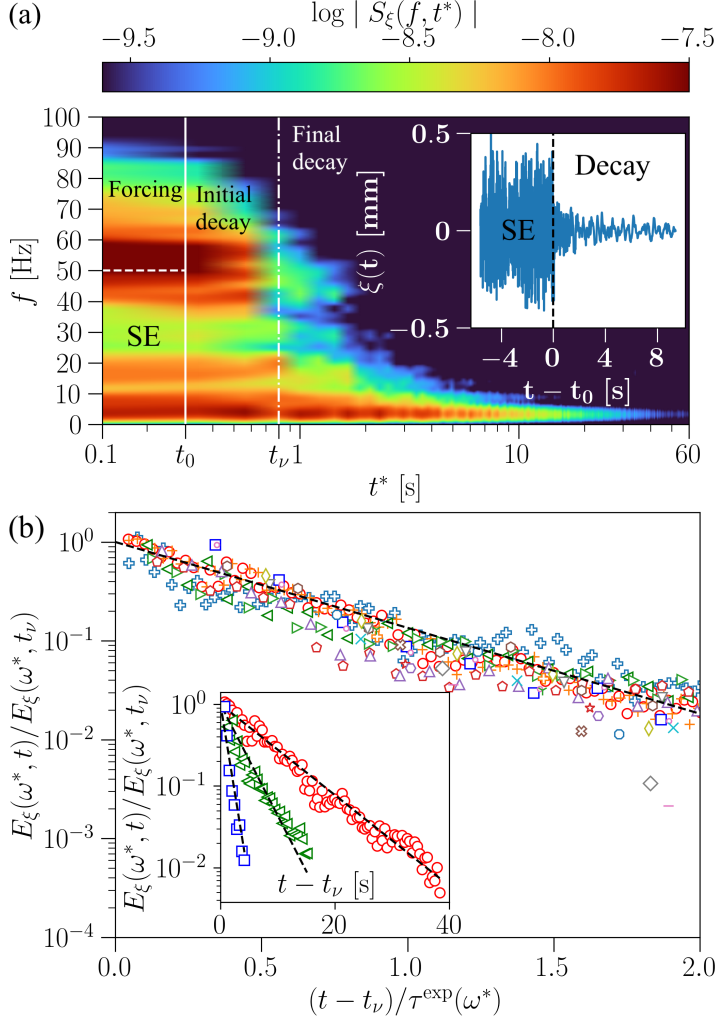
Figure 3: (a) Spectrogram $S_\xi(f,t^*)$ of the wave amplitude versus time t^* (log-scale) and frequency f. Log-scale colorbar. For $t < t_0$: small-scale forcing ($f_P \in [50, 100]$ Hz) and SE regime at large scales [$f < \min(f_P)$]. Forcing is stopped at time t_0 (vertical white solid line). For $t_0 \leqslant t < t_\nu$: initial decaying regime. Final decay starts at time t_ν (vertical white dot-dashed line). Applied tension $T = 6.8$ N m^{-1}. Inset: temporal decay of wave amplitude $\xi(t)$ before ($t < t_0$) and after ($t > t_0$) forcing stops. (b) Normalized energy spectrum versus the normalized time $(t-t_\nu)/\tau^{\exp}(\omega^*)$ for various Fourier modes $\omega^*/(2\pi) \in [2, 70]$ Hz (symbols). The black dashed line has a -2 slope corresponding to the exponential decay of Eq. (3.6). Applied tension $T = 5$ N m^{-1}. Inset: Normalized energy spectrum versus unrescaled time $t - t_\nu$ for Fourier modes $\omega^*/(2\pi) = 3.2(\circ)$, 6.4 ($\triangleleft$), and 20 ($\square$) Hz.

over a short time scale $\delta t = 0.5$ s. Figure 3a shows a typical example of a spectrogram, $S_\xi(\omega, t^*)$, averaged over 60 iterations. The horizontal white dashed line corresponds to the lower bound of the forcing frequency range, $\min(f_P)$. The vertical solid line at $t^* = t_0$ indicates the time at which the external forcing is turned off. When the forcing is on ($t^* < t_0$), the energy is well spread over all frequencies lower than the forcing ones $f < f_P$ (as in the inset of figure 2) where SE is commonly established (Vernet & Falcon 2025). After external forcing is switched off and final decay is initiated ($t^* > t_\nu$), all modes decay at different rates that depend on their frequency.
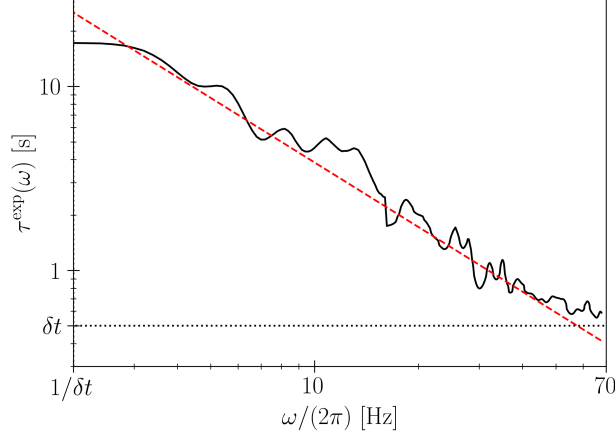
Figure 4: Experimental dissipation time scale $\tau^{\exp}(\omega)$ of hydroelastic tensional waves versus frequency $\omega/(2\pi)$. The red dashed line corresponds to Eq. (3.11) with no fitting parameter. Horizontal dotted line: temporal cutoff due to the spectrogram computation (short time interval $\delta t = 0.5$ s). Cutoff frequency: $1/\delta t = 2$ Hz. Applied tension $T = 5$ N m^{-1}.

The decay of the energy spectrum is then experimentally inferred from the link between the energy spectrum and the wave-amplitude power spectrum as $E_\xi(\omega,t) = (T/\rho)^{1/3}\omega^{4/3}S_\xi(\omega,t)$ (see Sect. 3.2). The inset of figure 3b shows that the energy spectrum $E_\xi(\omega^*,t)$ decays exponentially over time, and that its decay rate, $1/\tau^{\exp}(\omega^*)$ (i.e., the dashed-line slope), depends on the frequency mode ω^*. Each Fourier mode ω^* corresponds to a horizontal line in the spectrogram in figure 3a. When the energy spectrum $E_\xi(\omega^*,t)$, normalized by its value at $t = t_\nu$, $E_\xi(\omega^*,t_\nu)$, is plotted as a function of a normalized time $(t - t_\nu)/\tau^{\exp}(\omega^*)$, all data for various modes ω^* collapse on a master curve, as shown in the main figure 3b. A clear exponential decay is observed up to $(t - t_\nu)/\tau^{\exp}(\omega^*) \simeq 2$ showing thus that Eq. (3.6) is validated experimentally. The dissipation time scale can thus be directly obtained from Eq. (3.6) as $\tau^{\exp}(\omega^*) = 2\int_0^{+\infty} E_\xi(\omega^*,t)/E_\xi(\omega^*,t_\nu)dt$ due to the exponential nature of the decay.

Figure 4 then shows the experimental dissipation time scale as a function of the frequency. The prediction of Eq. (3.11) (red dashed line in figure 4) is well verified over the available frequency range with no fitting parameter. This frequency-scaling law has been checked for different tension values, but the small range of accessible tension and the weak exponent make it difficult to verify experimentally the $\tau \propto T^{1/3}$ scaling of Eq. (3.11). As the computation relies on the spectrogram $S_\xi(\omega,t^*)$, the moving integration time $\delta t = 0.5$ s is thus a lower bound for $\tau(\omega)$ as faster fluctuations are averaged. Decreasing further the value of δt presents also two drawbacks: (i) as $S_\xi(\omega,t^*)$ converges for $f > 1/\delta t$, so $\tau(\omega)$ can be computed only above this cutoff frequency, (ii) decreasing further δt also leads to noisier spectra. This method thus estimates τ for $1/\delta t < f < 60$ Hz, which is sufficient as the SE regime was initially established for frequencies lower than the forcing range $[50, 100]$ Hz.

3.5. *Temporal decay of energy*

Figure 5 shows the energy spectral density $E_\xi(\omega,t^*)$ at different decay times. Before the final decay ($t_0 \leqslant t < t_\nu$), statistical equilibrium of large scales is observed in reasonable agreement with the stationary prediction of Eq. (3.3) (top black dashed line) and the corresponding frequency power-law exponent $\alpha = 1/3$. When the final decay starts ($t > t_\nu$), the stationary SE regime rapidly collapses due to spectral dissipation and the absence of energy flux. Indeed,
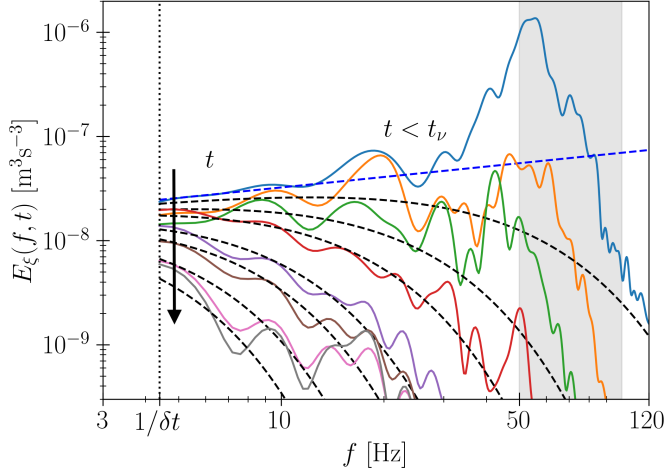
Figure 5: Energy spectrum $E_\xi(\omega, t)$ at different times, before ($t < t_\nu$ - top blue curve) and after ($t > t_\nu$ - other curves) the final decay starts. Obtained from vibrometer measurements at times $t - t_\nu \in [-0.4, 0.04, 0.7, 1.3, 2.9, 4, 6.2, 8.4]$ s (from top to bottom). The arrow indicates the direction of time. Black dashed lines correspond to Eq. (3.6) for the same times, except the blue dashed line, for $t - t_\nu = -0.4$ s (i.e., $t - t_0 = 0.1$ s), corresponding to Eq. (3.3). Black dotted line: cutoff frequency, $1/\delta t$, due to the spectrogram computation (short time interval of $\delta t = 0.22$ s). Grey region: initial forcing range, $f_p \in [50, 100]$ Hz. Applied tension $T = 6.8$ N m^{-1}.

all Fourier modes decay at different rates with $\tau^{-1}(\omega) \propto \omega^{7/6}$ [see Sect. 3.4, figure 4 and Eq. (3.11)], and thus modes of higher frequency decay faster than large-scale modes. Such a collapse of the spectrum is reasonably well captured by Eq. (3.6) (see black dashed lines in figure 5) with no fitting parameter. As discussed in Sect 3.2, since $\alpha = 1/3$ and $\beta = 7/6$, the energy stored in large-scale tensional waves is predicted to decay following Eq. (3.8) with $\delta = (\alpha + 1)/\beta = 8/7$, thus as Eq. (3.10) in $\mathcal{E}^\omega(t) \propto (t - t_\nu)^{-8/7}$.

Such a free decay of Fourier mode energy is experimentally studied using the temporal signal $\xi(t)$ measured at a given location by laser vibrometry. As the wave-amplitude spectrum S_ξ is related to the energy spectrum E_ξ by $E_\xi(\omega, t^*) = \omega^2 S_\xi(\omega, t^*)/k$, we obtain $\mathcal{E}^\omega(\omega, t^*)$ from the dispersion relation and the spectrogram $S_\xi(\omega, t^*)$ over a short-time window $\delta t = 0.22$ s as

$$\mathcal{E}^\omega(t^*) \equiv \int_{2\pi/\delta t}^{\omega_c} \frac{T}{\rho} k^2 S_\xi(\omega, t^*) d\omega, \tag{3.13}$$

with $\omega_c/(2\pi) = 30$ Hz as SE is reasonably established for $t \lesssim t_\nu$ up to this frequency.

To increase the statistical reliability of experimental data for $\mathcal{E}^\omega(t^*)$, measurements are performed over 60 decay experiments of 60 s each. Between each decay, forcing is maintained over 60 s long enough to recover a steady SE regime.

Figure 6a shows the temporal evolution of the total energy $\mathcal{E}^\omega(t)$, computed from Eq. (3.13), slightly before stopping forcing ($t < t_0$), where a steady SE regime occurs, and, after stopping ($t > t_0$), where the decay is observed during 30 s. Before collapsing, the SE prediction is maintained over a short period of time ($t_\nu - t_0 \sim 0.5$ s, i.e., 2 to $3\delta t$) during an initial period of decay. A final decay ($t > t_\nu$) then occurs during roughly 20 s. The main figure 6b then shows the temporal decay of $\mathcal{E}^\omega(t)$ in a log-log plot. $\mathcal{E}^\omega(t)$ shows a time power-law decay well described, over almost two decades, by the prediction of Eq. (3.10) in $(t - t_\nu)^{-8/7}$ (red-dashed line), up to $t - t_\nu \sim 20$ s. Note this self-similar decay does not rely on a self-similar spectrum during the decay (see figure 5). Similar results have been obtained
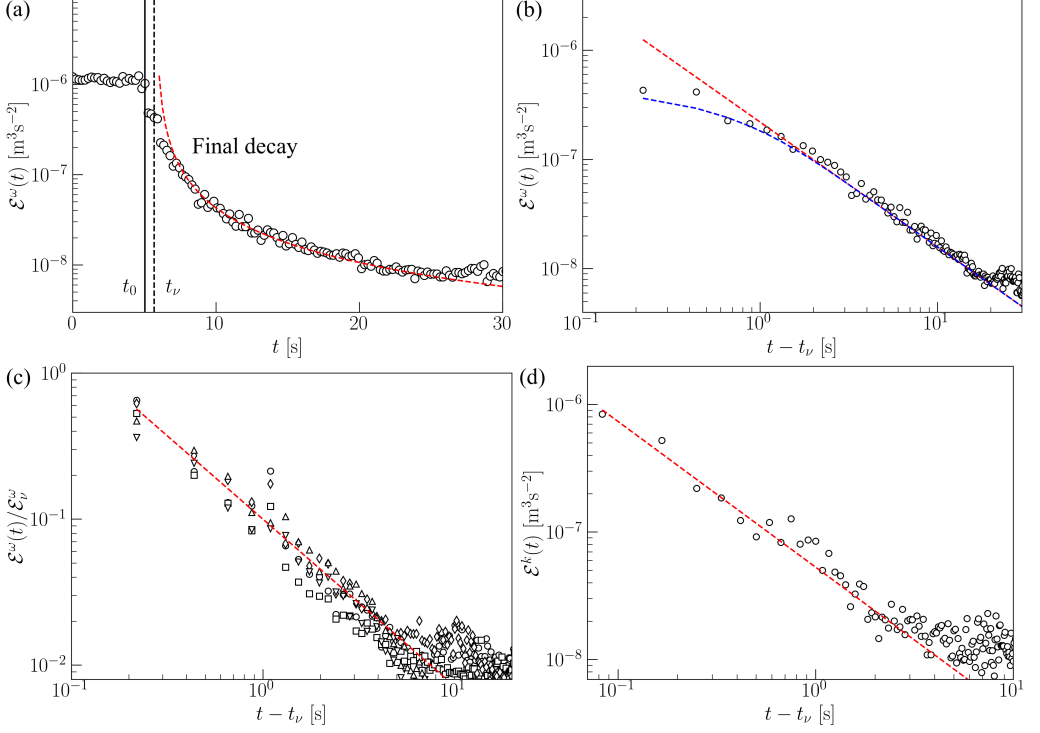
Figure 6: (a) Temporal evolution (semilog-y plot) of the total energy $\mathcal{E}^\omega(t)$ before ($t < t_0$) and after ($t > t_0$) forcing stops. Vertical solid line corresponds to $t = t_0$. Vertical dashed line corresponds to the start of the final decay at $t = t_\nu$. The initial decay lasts $t_\nu - t_0 \simeq 0.5$ s and the final decay of the order of 20 s. (b) Temporal decay of the total energy $\mathcal{E}^\omega(t)$, estimated by laser vibrometry and averaged over 60 decay experiments. Red-dashed line has a $-8/7$ slope corresponding to the prediction of Eq. (3.10). Full prediction of Eq. (3.8) corresponds to the blue-dashed line. Applied tension: $T = 6.8$ N m^{-1}. (c) $\mathcal{E}^\omega(t)$ rescaled by its initial value for various initial forcing strengths $E_0 \in [1.5, 15] \times 10^{-8}$ m^3.s^{-2} (from $\circ$- to $\triangle$-symbols). Red-dashed line has a $-8/7$ slope [Eq. (3.10)]. (d) Temporal decay of the total energy $\mathcal{E}^k(t)$ estimated by FTP. Red-dashed line has a $-8/7$ slope [Eq. (3.10)]. Applied tension $T = 6.8$ N m^{-1}.

at different measurement locations and for different applied tensions $T \in [3, 7]$ N m^{-1}. Moreover, the $-8/7$ exponent is independent of the strength of the initially applied forcing, thus for different energies $\mathcal{E}^\omega(t = t_\nu)$ of the initial SE regime (see figure 6c), as expected by Eq. (3.10). Note that only the total duration of the decay is modified. As detailed in Sect. 3.3, the time power-law prediction of Eq. (3.10) is accurate only for $t - t_\nu > \tau_c$ with $\tau_c \sim 0.3 - 0.5$ s. As shown in figure 6b, the full prediction of Eq. (3.8) (blue-dashed line) departs from this time power law only for $(t - t_\nu)/\tau_c \lesssim 2$, i.e., $(t - t_\nu) \lesssim 1$ s.

Finally, let us use the spatiotemporal measurements of $\eta(x, y, t)$ obtained by FTP to probe the energy decay in the spatial Fourier space $\mathcal{E}^k(t)$. We expect that the energy decay, computed with the two different methods, will be the same, i.e., $\mathcal{E}^\omega(t) = \mathcal{E}^k(t)$. The total energy $\mathcal{E}^k(t)$ is then defined by

$$\mathcal{E}^k(t) = \int_{k_\mathcal{L}}^{k_c} \frac{T}{\rho} k^2 \langle \tilde{S}_\eta(k, t) \rangle_{\delta\tau} dk, \tag{3.14}$$

where $k_c = k(\omega_c)$, $k_\mathcal{L} = 2\pi/\mathcal{L}$, and $\tilde{S}_\eta(k, t) = \langle |\breve{\eta}(k, \varphi, t)|^2 \rangle_\varphi / \mathcal{L}^2$ is the spatial power spectrum of the wave amplitude, $\breve{\eta}(k, \varphi, t)$ is the spatial Fourier transform of $\eta(x, y, t)$, and $\langle \cdot \rangle_{\delta\tau}$ denotes a temporal average over a short time window $\delta\tau = 8.3 \times 10^{-2}$ s to slightly

smooth the spectrum fluctuations. Figure 6d then shows the temporal decay of the total energy, $\mathcal{E}^k(t)$, computed from Eq. (3.14) over the spatial scales fulfilling SE, i.e., from $k_{\mathcal{L}}$ to k_c. Here also, $\mathcal{E}^k(t)$ shows a power-law decay well described, over almost two decades, by the prediction of Eq. (3.10) in $(t - t_\nu)^{-8/7}$ (red-dashed line). After a typical time $t - t_\nu \sim 4$ s, the spatiotemporal measurement reaches a signal-to-noise ratio close to unity. The duration of decay (~ 20 s) is longer using local vibrometry measurements due to its better vertical resolution. Overall, both methods converge to the same decaying exponent $-8/7$ predicted by Eq. (3.10) during the final decay.

4. Conclusions

We experimentally reported on the free decay of large-scale hydroelastic turbulent waves, initially in a state of statistical equilibrium (SE) where energy is equipartitioned among large-scale modes. Using space- and time-resolved measurements, we showed that the total energy of such large-scale tensional waves decays over time as $\mathcal{E}(t) \propto (t - t_\nu)^{-8/7}$, where t_ν denotes the start of the final decay. We derived the energy decay law from the theoretical SE spectrum and linear viscous damping. This prediction is in good agreement with experimental data over nearly two decades in time, for various initial energy inputs of the SE state. We also identified the dissipation mechanism as arising from a zero horizontal velocity boundary condition at the sheet-liquid interface, and confirmed the predicted dissipation rate $\tau(\omega)$ experimentally over more than a decade in frequency. To our knowledge, this represents the first experimental validations of both $\mathcal{E}(t)$ and $\tau(\omega)$ for hydroelastic tensional waves. Our approach is broadly applicable to other decaying turbulence or wave-turbulence systems initially in a large-scale SE regime.

Once forcing is stopped, a short initial decay driven by nonlinearities occurs before a long viscous final decay initiates. Within this final decay, each energy Fourier mode decays over a different timescale, leading to a rapid breakdown of the SE regime as high-frequency (i.e., small-scale) modes dissipate faster. This collapse of SE prevents the definition of effective temperature and entropy, which are only meaningful in the stationary regime (Vernet & Falcon 2025). Although weak dissipation allows SE to form under steady forcing, it dominates once the final decay starts, making statistical mechanics inapplicable. Still, the energy decay retains a memory of the initial SE through its influence on the time power-law decay exponent of the total energy. This behavior contrasts with classical wave turbulence, where energy stored in the largest scale continues to cascade toward smaller scales during decay, preserving a self-similar spectrum at early time (Deike et al. 2012; Cazaubiel et al. 2019). The scenario described here is thus the wave turbulence counterpart of the free decay of large-scale SE in 3D turbulence reported by Gorce & Falcon (2024).

Although our experimental system focuses on tensional waves, i.e., hydroelastic waves that differ from the bending-dominated regime relevant to ice floes, these two systems share several common properties. Both tensional and bending waves exhibit three-wave resonant interactions, which thus inhibit an inverse cascade of energy, making the SE regime relevant for large-scale turbulent bending waves. Moreover, the dissipation mechanism identified here should also apply to the sea-ice case, although whether it is the dominant pathway for energy dissipation remains unclear. This question is still open in geophysics and lies beyond the scope of the present study.

Finally, several questions remain open when considering nonstationary processes. Namely, what is the mechanism behind the emergence of SE? What is the SE dynamics when the external random forcing is slowly modulated in time? From a broader perspective, and for the steady SE regime, how far can the analogy to statistical mechanics be pushed? For instance, is there a possibility for the Fluctuation Theorem and the Fluctuation-Dissipation relation to

hold in these systems in SE? Answering these questions using statistical mechanics concepts would undoubtedly strengthen our understanding of the large scales of turbulent systems in SE.

Acknowledgement

Funding

Declaration of interests

The authors declare no conflicting interests.

REFERENCES

BATCHELOR, G. K. 1953 *The Theory of Homogeneous Turbulence*. Cambridge University Press, New York.

BAUDIN, K., FUSARO, A., KRUPA, K., GARNIER, J., RICA, S., MILLOT, G. & PICOZZI, A. 2020 Classical Rayleigh-Jeans condensation of light waves: observation and thermodynamic characterization. *Phys. Rev. Lett.* **125**, 244101.

BEDARD, R., LUKASCHUK, S. & NAZARENKO, S. 2013 Non-stationary regimes of surface gravity wave turbulence. *JETP Lett.* **97**, 459–465

BERESNYAK, A. & LAZARIAN, A. 2008 Wave decay in magnetohydrodynamic turbulence. *Astrophys. J.* **678**, 961.

BETTEGA, G. & ROMAN, H. E. 2009 Wavelet analysis of two-dimensional turbulence in a pure electron plasma. *Europhys. Lett.* **85**, 35001.

BIGOT, B., GALTIER, S. & POLITANO, H. 2008 Energy decay laws in strongly anisotropic magnetohydrodynamic turbulence. *Phys. Rev. Lett.* **100**, 074502.

CAZAUBIEL, A., MAWET, S., DARRAS A., GROJEAN G., VAN LOON J.J.W.A., DORBOLO, S. & FALCON, E. 2019 Wave turbulence on the surface of a fluid in a high-gravity environment. *Phys. Rev. Lett.* **123**, 244501

CIEŚLIK, A. R., KAMP, L. J., CLERCX, H. J. H. & VAN HEIJST, G. J. F. 2009 Meandering streams in a shallow fluid layer. *Europhys. Lett.* **85**, 54001.

COBELLI, J., MAUREL, A., PAGNEUX, V. & PETITJEANS, P. 2009 Global measurement of water waves by Fourier transform profilometry. *Exp. Fluids* **46**, 1037–1047.

COMTE-BELLOT, G. & CORRSIN, S. 1966 The use of a contraction to improve the isotropy of grid-generated turbulence. *J. Fluid Mech.* **25**, 657–682.

DAS, S., SAHOO, T. & MEYLAN, M. H. 2018 Dynamics of flexural gravity waves: from sea ice to Hawking radiation and analogue gravity. *Proc. R. Soc. A: Math. Phys. Eng. Sci.* **474**(2209), 20170223.

DAVYS, J. W., HOSKING, R. J. & SNEYD, A. D. 1985 Waves due to a steadily moving source on a floating ice plate. *J. Fluid Mech.* **158**, 269–287.

DEIKE, L., BACRI, J.-C. & FALCON, E. 2013 Nonlinear waves on the surface of a fluid covered by an elastic sheet. *J. Fluid Mech.* **733**, 394–413.

DEIKE, L., BERHANU, M. & FALCON, E. 2012 Decay of capillary wave turbulence. *Phys. Rev. E* **85**, 066311.

DEIKE, L., MIQUEL, B., GUTIÉRREZ, P., JAMIN, T., SEMIN, B., BERHANU, M., FALCON, E. & BONNEFOY, F. 2015 Role of the basin boundary conditions in gravity wave turbulence. *J. Fluid Mech.* **781**, 196–225.

DELORY, A., KIEFER, D. A., LANOY, M., EDDI, A., PRADA, C. & LEMOULT, F. 2024 Viscoelastic dynamics of a soft strip subject to a large deformation. *Soft Matter* **20**, 1983–1995.

FALKOVICH, G. E., SHAPIRO, I. YA & SHTILMAN, L. 1995 Decay Turbulence of Capillary Waves. *Europhysics Letters* 29, 1–6.

14

GORCE, J.-B. & FALCON, E. 2022 Statistical equilibrium of large scales in three-dimensional hydrodynamic turbulence. *Phys. Rev. Lett.* **129**, 054501.

GORCE, J.-B. & FALCON, E. 2024 Freely decaying Saffman turbulence experimentally generated by magnetic stirrers. *Phys. Rev. Lett.* **132**, 264001.

HENDERSON, D. M. & MILES, J. W. 1990 Single-mode Faraday waves in small cylinders. *J. Fluid Mech.* **213**, 95–109

KOLMAKOV, G. V., LEVCHENKO, A. A., BRAZHNIKOV, M. YU., MEZHOV-DEGLIN, L. P., SILCHENKO, A. N. & MCCLINTOCK, P. V. E. 2004 Quasiadiabatic decay of capillary turbulence on the charged surface of liquid hydrogen. *Phys. Rev. Lett.* **93**, 074501.

LAMB, H. 1932 *Hydrodynamics.* Dover, New York.

LANDAU, L. D. & LIFSHITZ, E. M. 1970 *Theory of Elasticity.* 2nd Ed., Pergamon Press, London.

MARCHENKO, A. V. & SHRIRA, V. I. 1991 Theory of two-dimensional nonlinear waves in liquid covered by ice. *Fluid Dyn.* **26**, 580–587.

MARTIN, B. K., WU, X. L., GOLDBURG, W. I. & RUTGERS, M. A. 1998 Spectra of decaying turbulence in a soap film. *Phys. Rev. Lett.* **80**, 3964.

MICHEL, G., PÉTRÉLIS, F. & FAUVE, S. 2017 Observation of thermal equilibrium in capillary wave turbulence. *Phys. Rev. Lett.* **118**, 144502.

MILES, J. W. 1967 Surface-wave damping in closed basins. *Proc. R. Soc. Lond. A* **297**, 459–475.

MIQUEL, B. & MORDANT, N. 2011 Nonlinear dynamics of flexural wave turbulence. *Phys. Rev. E* **84**, 066607.

MIQUEL, B., NAERT, A. & AUMAÎTRE, S. 2021 Low-frequency spectra of bending wave turbulence. *Phys. Rev. E*, **103**, L061001.

MORIZE, C. & MOISY, F. 2006 Energy decay of rotating turbulence with confinement effects. *Phys. Fluids* **18**, 065107.

ONORATO, M., OSBORNE, A. R., SERIO, M., RESIO, D., PUSHKAREV, A., ZAKHAROV, V. E. & BRANDINI, C. 2002 Freely decaying weak turbulence for sea surface gravity waves. *Phys. Rev. Lett.* **89**, 144501.

PAN, Y. & YUE, D.K.P. 2015 Decaying capillary wave turbulence under broad-scale dissipation. *J. Fluid Mech.* **780**, R1

PĂRĂU, E. I., ȚUGULAN, C., TRICHTCHENKO, O. & ALBERELLO, A. 2024 Flexural-Gravity Waves Under Ice Plates and Related Flows. *Nonlinear Disp. Waves*, edited by D. Henry (Birkhäuser, Cham), 173–200.

SAFFMAN, P. G. 1967 The large-scale structure of homogeneous turbulence. *J. Fluid Mech.* **27**, 581–593.

SCHULKES, R. M. S. M., HOSKING, R. J. & SNEYD, A. D. 1987 Waves due to a steadily moving source on a floating ice plate. Part 2. *J. Fluid Mech.* **180**, 297–318.

SHATS, M., BYRNE, D. & XIA, H. 2010 Turbulence decay rate as a measure of flow dimensionality. *Phys. Rev. Lett.* **105**, 264501.

SKRBEK, L. & SREENIVASAN, K. R. 2012 Developed quantum turbulence and its decay. *Phys. Fluids* **24**, 011301.

SQUIRE, V. A., VAUGHAN, G. L. & BENNETS, L. G. 2009 Ocean surface wave evolvement in the Artic Basin. *Geophys. Res. Lett.* **36**, L22502

SUN, C., JIA, S., BARSI, C., RICA, S., PICOZZI, A. & FLEISCHER, J. W. 2012 Observation of the kinetic condensation of classical waves. *Nature Phys.* **8**, 470–474.

SUTHERLAND, G. & RABAULT, J. 2016 Observations of wave dispersion and attenuation in landfast ice. *J. Geophys. Res.: Oceans* **121**, 1984–1997.

VAN DORN, W. G. 1966 Boundary dissipation of oscillatory waves. *J. Fluids Mech.* **24**, 769–779

VERNET, M. & FALCON, E. 2025 Thermodynamics and Statistical Equilibrium of Large-Scale Hydroelastic Wave Trubulence. *Phys. Rev. Lett.* **135**, 024004.

WANG, C. M., WATANABE, E. & UTSUNOMIYA, T. 2008 *Very Large Floating Structures.* Taylor and Francis, New York.

YANG, Y. & HUANG, L. 2024 Waves and structural strain induced by a uniform current flow underneath a semi-infinite floating solar coverage. *Phys. Rev. Fluids* **9**, 094804.

YOKOYAMA N. 2004 Statistics of gravity waves obtained by direct numerical simulation. *J. Fluids Mech.* **501**, 169-178.

ZAKHAROV, V. E., LVOV, V. & FALKOVICH, G. 2025 *Kolmogorov-Zakharov Spectra of Turbulence: Wave turbulence.* Springer, Cham.

ZHANG Z. & PAN, Y. 2022 Numerical investigation of turbulence of surface gravity waves. *J. Fluids Mech.* **933**, A58